doi:10.1093/brain/awn114 *Brain* (2008), **131**, 1990–2001

Mutation of *FIG4* causes a rapidly progressive, asymmetric neuronal degeneration

Xuebao Zhang,[1] Clement Y. Chow,[2] Zarife Sahenk,[3,4] Michael E. Shy,[1] Miriam H. Meisler[2] and Jun Li[1,5]

[1]Department of Neurology, Wayne State University, School of Medicine, Detroit, MI, [2]Department of Human Genetics, University of Michigan, Ann Arbor, MI, [3]Columbus Children's Research Institute, [4]Department of Neurology, Ohio State University, Columbus, OH and [5]John D. Dingell VA Medical Center, Detroit, MI, USA

Correspondence to: Jun Li, MD, PhD, Department of Neurology, Wayne State University School of Medicine, Detroit, MI 48201
E-mail: junli@med.wayne.edu

Recessive Charcot-Marie-Tooth disease type-4J (CMT4J) and its animal model, the pale tremor mouse (*plt*), are caused by mutations of the *FIG4* gene encoding a PI(3,5)P_2 5-phosphatase. We describe the 9-year clinical course of CMT4J, including asymmetric, rapidly progressive paralysis, in two siblings. Sensory symptoms were absent despite reduced numbers of sensory axons. Thus, the phenotypic presentation of CMT4J clinically resembles motor neuron disease. Time-lapse imaging of fibroblasts from CMT4J patients demonstrates impaired trafficking of intracellular organelles because of obstruction by vacuoles. Further characterization of *plt* mice identified axonal degeneration in motor and sensory neurons, limited segmental demyelination, lack of TUNEL staining and lack of accumulation of ubiquitinated protein in vacuoles of motor and sensory neurons. This study represents the first documentation of the natural history of CMT4J. Physical obstruction of organelle trafficking by vacuoles is a potential novel cellular mechanism of neurodegeneration.

Keywords: *FIG4* or *SAC3* gene; PI(3,5)P2-5-phosphatase; neuronopathy; axonal degeneration; vacuoles; amyotrophic lateral sclerosis; motor neuron disease; segmental demyelination; Schwann cells

Abbreviations: CMT4BI = Charcot-Marie-Tooth type 4BI; CMT4J = Charcot-Marie-Tooth disease type-4J; DRG = dorsal root ganglion; EMG = electromyogram; IHC = immunohistochemistry; MAG = myelin-associated glycoprotein; MND = motor neuron disease; NCS = nerve conduction studies; NF = neurofilament; NFp = phosphorylated neurofilaments; VAPB = vesicle-associated membrane protein-associated protein-B; VCP = valosin-containing protein

Received March 21, 2008. Revised May 2, 2008. Accepted May 12, 2008. Advance Access publication June 12, 2008

Introduction

Phosphoinositides regulate intracellular membrane trafficking by recruiting effector proteins to the surface of specific organelles (Bolis *et al.*, 2007; Volpicelli-Daley *et al.*, 2007). The levels of phosphoinositides are regulated by specific kinases and phosphatases (Di Paolo *et al.*, 2006; Volpicelli-Daley *et al.*, 2007). Phosphoinositide signalling is particularly important for the integrity of the nervous system. Mutations in *MTMR2* and *MTMR13*, which dephosphorylate PI3P and PI(3,5)P_2 at the 3rd position of inositol, cause the recessive inherited neuropathies Charcot-Marie-Tooth type 4B1 (CMT4B1) and CMT4B2, with a distinctive pathology of excessive myelin out-folding. Mutations of FIG4/SAC3 were recently shown to cause Charcot-Marie-Tooth type 4J (CMT4J), as discussed below.

FIG4/SAC3 is a phosphatase that dephosphorylates PI(3,5)P_2 at the 5th position of inositol (Duex *et al.*, 2006*b*; Chow *et al.*, 2007). FIG4 interacts with FAB1 and VAC14 in a protein complex that regulates the overall concentration of PI(3,5)P_2 (Di Paolo *et al.*, 2006; Sbrissa *et al.*, 2007). Although the detailed molecular mechanism of this regulation remains to be clarified, loss of function of *FIG4* reduces the levels of PI(3,5)P_2 (Duex *et al.*, 2006*a*, *b*; Chow *et al.*, 2007). We recently described a mouse mutant, pale tremor (*plt*), with a spontaneous mutation that eliminates the expression of *FIG4*. Homozygous *plt* mice have a neuronopathy with extensive neuronal degeneration in the central and peripheral nervous systems, including loss of dorsal root ganglion (DRG) neurons and large myelinated axons in the sciatic nerve. A screen of 95 patients with CMT identified four patients with mutations in *FIG4* (Chow *et al.*, 2007). The natural history and pathogenesis of CMT4J has not been well characterized. In this report, we provide evidence that CMT4J is a primary neuronopathy.

Patients develop rapidly progressive, asymmetric motor neuron degeneration without symptoms of sensory loss, although both sensory and motor neurons exhibit morphological abnormalities. Abnormal transport of intracellular organelles was observed by time-lapse imaging in fibroblasts from CMT4J patients. The data provide insights into the pathogenesis of CMJ4J and the pattern of disease progression in motor neuron disease (MND).

Methods

Plt mice and genotyping

The *plt* mutation was genotyped by PCR as previously described (Chow *et al.*, 2007). Eleven mice were examined at 6 weeks of age and two mice at 3 weeks of age.

Semithin section and EM

Mice were transcardially perfused with 4% paraformaldhyde and 3.5% glutaraldhyde. Sciatic nerve and dorsal/ventral roots were dissected and post-fixed for 24 h. Nerves were then osmicated for 1.5 h, dehydrated and embedded in Epon. Tissue blocks were sectioned with 1 μm thickness and stained with methylene blue for light microscopic examination. The blocks were then trimmed and sectioned into ultrathin sections for EM examination (Zeiss EM 900). The same methods were applied to patients' sural nerve.

Morphometric analysis

Semithin sections of dorsal and ventral roots of *plt* mice. (thickness = 1 μM) were examined under the 63X objective. We imaged *the entire* field of transverse sections of each lumbar root for analysis. Images were imported into morphometric software (ImagePro Plus). Areas of each field were counted to obtain nerve fibre density, myelin thickness, *g*-ratio and histograms.

Teased nerve fibre immunohistochemistry (IHC)

Nerves were fixed in 4% paraformaldehyde for 30 min after dissection from perfused mice. Sciatic nerves were teased into individual fibres on glass slides. The slides were dried overnight, reacted with primary antibodies, and stored at 4°C overnight, then incubated for 2 h with secondary antibodies. The stained slides were examined under a Leica fluorescent microscope.

Patients

We evaluated two siblings, a male of current age 44 years (patient 1) and his sister of 46 years (patient 2). These patients, designated BAB1372 and BAB1373 in reference Chow *et al.*, are compound heterozygotes for mutations of *FIG4*, R183X in exon 6 and I41T in exon 2. Detailed medical histories were obtained and serial neurological examinations were performed, followed by electrophysiological studies below.

Electromyogram/nerve conduction studies

Nerve conduction studies (NCS) of median, ulnar, peroneal, tibial and sural nerves were performed using conventional methods. The distal stimulation distances for motor conduction studies were 7 cm in the arms and 9 cm in the legs. A concentric electromyogram (EMG) needle was used and recordings were made at standard settings (Li *et al.*, 2002).

Skin biopsy and human fibroblast culture

Punch skin biopsies were obtained from patients, rinsed with PBS, minced into coarse slurry using an iris scissor and transferred into a 15 ml plastic tube containing 4 mg/ml collagenase II in basal medium eagle with 20% foetal bovine serum and 100 IU/ml penicillin–streptomycin. The tube was placed in incubator at 37°C for 24 h and centrifuged at 1000 rpm for 5 min next day. Supernatants were removed using a pipette. Pellets were washed twice with PBS, suspended in 1 ml basal medium eagle medium and transferred into a flask to be distributed over the bottom surface. The flask was placed in a humidified 5% CO_2 incubator at 37°C. Cells were passaged by removing the media, washing with calcium- and magnesium-free PBS and incubated with 0.25% trypsin-EDTA in PBS for 3–5 min. The action of trypsin was terminated by adding medium containing 20% foetal bovine serum. After centrifugation, pelleted cells were washed with PBS and resuspended. The suspension was split into thirds for seeding. Cultures were passaged approximately every other week. Cultures were examined under light microscopy. All experiments were conducted between passages 3 and 8. Control and mutant cells were compared at the same passage.

IHC, TUNEL staining and proliferation assay

IHC

Mice were transcardially perfused with 4% paraformaldhyde. Dissected nerves were fixed overnight at 4°C in fresh 4% paraformaldehyde and cryoprotected in PBS containing 20% sucrose. Tissues were embedded in OCT, sectioned into 10 μm thickness slices in a cryostat, and thaw-mounted onto Superfrost Plus slides (Fisher Scientific, PA). After drying, sections were washed in PBS, permeabilized with cold acetone in −20°C, blocked for 1 h in blocking solution (0.5% Triton-X-100 fish gelatin solution in PBS) and incubated overnight at 4°C with primary antibodies (Table 1); followed by secondary antibody for 2 h at room temperature. After washing with PBS, sections were dried and coversliped. For teased nerve fibre IHC, dissected nerves were post-fixed in 4% paraformaldehyde for 30 min and teased into individual fibres on slides. Teased fibres were dried overnight and immunostained as described (Bai *et al.*, 2006; Li *et al.*, 2006). The stained slides were examined using a fluorescent microscope (Leica Microsystems, Germany).

TUNEL staining and proliferation assay

Apoptosis was evaluated by TUNEL using a ApopTag® Plus Fluorescein *In-Situ* Apoptosis Detection Kit (Chemicon, Illinois, USA) according to the manufacturer's protocol. Briefly, cryostat sections, 10 μM thickness, were washed in PBS for 5 min and post-fix in pre-cooled ethanol: acetic acid 2 : 1 for 5 min at −20°C. Slides were first incubated with equilibration buffer, and then replaced with Working Strength TdT enzyme for 1 h at 37°C in a humidified chamber. The reaction was terminated by adding working strength stop/wash buffer. For the negative control, the TdT enzyme was replaced by equilibration buffer. Tissues were further incubated with warmed (RT) working strength antidigoxigenin conjugates for 0.5 h at RT. The nucleuses were counterstained by DAPI. For the proliferation assessment, antibody against Ki67 was used for IHC as described above. Neurons in the DRG, spinal cord anterior horn and Schwann cells in sciatic nerve were identified by antibodies against neurofilament (NF), ChAT

Table 1 Primary antibodies

Antibody	Source	Species raised in	Specific antigen	Type	Reference
α-Ubiquitin	Vector, CA Cat # VP-U576	Rabbit	Ubiquitin cross linked to limpet haemocyanin	Polyclonal IgG	Li *et al*. (2006)
SMI31	COVANCE # SMI31R	Mouse	NFP	Monoclonal IgG1	Giasson *et al*. (1996)
VCP	BioReagents # MA3-004	Mouse	A synthetic peptide corresponding to residues 792–806	Monoclonal IgG2a	Vij *et al*. (2006)
MAG	Zymed Laboratories # 34-6200	Rabbit	The shared C-terminal region of the small and large MAG	Polyclonal Antiserum	Yamamoto *et al*. (1994)
CD68	AbD Serotec # MCA1957	Rat	Macrosialin	Monoclonal IgG2a	da Silva *et al*. (1999)
Lamp2	USBiological # L9190-14A	Mouse	D107b	Monoclonal IgG1	Fanin *et al*. (2006)
EEA1	USBiological # E2211-01	Rabbit	EEA1	Polyclonal IgG	Mills *et al*. (1998)
NF-L	COVANCE # PRB-574C	Rabbit	Full length recombinant NF-L	Polyclonal Antiserum	Goldstain *et al*. (1991)
S-100	CHEMICON # AB941	Rabbit	Keyhole limpet hemocyanin (KLH) with carbodiimide	Polyclonal Antiserum	Gonzalez-Martinez *et al*. (2003)
ChAT	CHEMICON # AB144P	Goat	Choline acetyltransferase	Polyclonal Affinity purified immunoglobulin	Barber *et al*. (1984)
Ki67	DakoCytomation	Mouse	Bacterially expressed parts of hunan ki67 cDNA	Monoclonal IgG1	Muskhelishvili *et al*. (2003)

and S-100, respectively. Numbers of TUNEL-positive and total cells (neurons or Schwann cells) were counted under 40× lens in each section for apoptotic cells. Apoptotic index was expressed as the number of TUNEL-positive cells in total cell of 1000 for each mouse. The nucleus localization of TUNEL-positive signal was verified with double-stained of DAPI (Thompson *et al*., 2000).

Time-lapse imaging

Time-lapse recording was made under a phase contrast optic using a computer-assisted invert microscope (Olympus IX70). Temperature in the culture chamber was maintained at 37°C with a thermostat controller (MATS-U55R30, Tokai Hit Co., Japan). Images under a 40× or 60× lens were captured every 5 s through a CCD camera over 30–60 min. To stabilize CO_2 concentration during recording, culture medium was replaced with Leibovitz's L-15 medium containing 20% foetal bovine serum 2 h prior to imaging (Yan *et al*., 2007).

Results

Rapidly progressive and asymmetric paralysis in two patients with *FIG4* mutations

To characterize the natural history of patients with *FIG4* mutations, we followed two siblings with adult onset CMT4J for 9 years. Both patients are compound heterozygotes carrying the FIG4 protein truncation mutation R183X and the missense mutation I41T. Two patients with early-onset of CMT4J were not seen by us and were not included (Chow *et al*., 2007).

Patient 1

When first seen in 1998, the proband was a 37-year-old woman who had developed progressive right arm weakness over the course of 1 year following a fall from a desk in 1993. She was the product of a normal pregnancy and delivery, and walked at 9 months of age. She was a dancer as a child until the age of 13 when she was no longer able to dance on her toes. During several clinical visits, no obvious cognitive dysfunction was observed. She was a high school teacher until the severe paralysis developed. Her brain MRI was unremarkable. An examination in 2002 revealed no voluntary movements in the right upper extremity, which was diffusely atrophied. She also had mild weakness of her left upper limb (intrinsic hand muscles 1/5, deltoid 4+/5) and asymmetric, mild, weakness of her legs, with the right worse than the left (Supplementary Video 1). By June 2007, she had no voluntary movement of either arm or right leg (Supplementary Video 2). She had 4−/5 strength throughout the left leg. Her sensory examination was normal for pin prick and position sense. She had mild loss of vibration sense in the right hand. She was diffusely areflexic. The patient died of presumed respiratory compromise in February 2008.

Patient 2

The proband's brother (a computer programmer) was healthy until 1995 when his left leg gave way and he fell down the stairs. He walked by 1 year of age and participated in sports, at a varsity level, in high school. We evaluated him in 1998 at age 35 and then again in 2002 (Supplementary Video 3). In 2002, he had <3/5 strength in iliopsoas and quadriceps muscles bilaterally, but was able

Table 2 NCS/EMG[a] in patients with CMT4J

Nerves	CMAP/SNAP		DL (M/S)		CV (M/S)		*F*-wave Latency	
	1998	2007	1998	2007	1998	2007	1998	2007
Patient 1								
Median	2.0/8.0	nr/nr	10.3/3.9	nr/nr	19.8/34.8	nr/nr	67.9	nr
Ulnar	6.0/12.0	nr/nr	5.6/2.3	nr/nr	23.8/50.0	nr/nr	64.9	nr
Per EDB	0.8	nr	13.2	nr	8.1	nr	nr	nr
Tibial	2.0	nr	2.1	nr	8.3	nr	nr	nr
Sural	nr	nr	nr	nr	nr	nr		
Patient 2								
Median	11.2/26.6	7.3/3.8	4.7/2.8	6.5/2.8	46.7/50.0	36.0/39.0	37.0	40.4
Ulnar	11.7/22.3	9.7/nr	3.7/3.1	4.3/nr	50.0/45.1	35.0/nr	35.9	29.6
Per EDB	nr	nr	nr	nr	nr	nr	nr	nr
Per AT	3.3	nr	6.3	nr	46	nr	nr	nr
Sural	nr	nr	nr	nr	nr	nr		

[a]Needle EMG: abnormal spontaneous activities and reduced recruitment in all limbs.
CMAP = compound muscle action potential (mV); SNAP = sensory nerve action potential (μV); DL = distal latency (ms); M/S = motor nerve distal latency (ms)/sensory nerve distal latency (ms); CV = conduction velocity (m/s); nr = non-responsive; Per EDB = motor peroneal nerve recorded at the extensor digitorium brevis muscle; Per AT = motor peroneal nerve recorded at the anterior tibialis muscle.

to walk with assistance. Anterior tibialis strength was 1/5 bilaterally. Gastrocnemius strength was nearly normal (4+/5) of the right but only 1/5 on the left. Upper extremity strength was entirely normal. By 2007, he was confined to a wheel chair with no voluntary movement of any muscle in either leg (Supplementary Video 4). Strength was now reduced (4/5) in his left deltoid although distal muscles of this arm and all muscles of the *right* arm were still 5/5. On sensory examination, he had a mild decrease to vibration in the toes of both feet. Proprioception and pin prick sensation were normal in all limbs. He was diffusely areflexic. Like the proband, we found no obvious cognitive dysfunction. Neither patient had abnormalities of skin or hair colour.

NCS in both patients demonstrated that compound motor and sensory responses were asymmetric, severely reduced and progressed in severity between 1998 and 2007 (Table 2). There were prolonged distal latencies, significantly slowed conduction velocities and prolonged *F*-wave latencies in both patients. The NCS features suggest a demyelinating polyneuropathy in addition to severe axonal loss. Needle EMG showed abundant abnormal spontaneous activities (fibrillations and positive waves) in all limbs. Motor unit action potentials were of long duration and polyphasic with large amplitudes. The recruitment of these Motor unit action potentials was severely reduced. Taken together, the abnormalities suggested severe and widespread denervation, similar to that observed in patients with MND (Eisen, 2001). The denervation was severe in the proximal muscles, and, like the weakness, was asymmetric, suggestive of a neuronopathy but not length dependent axonal polyneuropathy.

A sural nerve biopsy was obtained from patient 2. Semithin sections and EM revealed severely reduced numbers of myelinated nerve fibres with a large amount of collagen in the extracellular matrix (Fig. 1). Onion bulbs and thinly myelinated nerve fibres were observed. Osmicated teased nerve fibres showed evidence of de- and re-myelination in 60% of the myelinated nerve fibres.

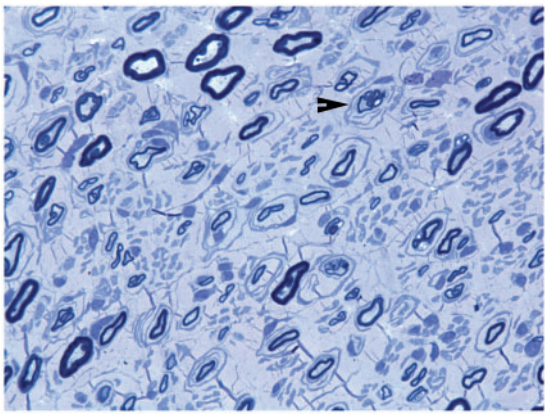

Fig. 1 Loss of myelinated nerve fibres in sural biopsy of a patient with CMT4J. A semithin section with toluidine blue staining was performed on the sural nerve biopsy of the patient 2. The number of myelinated nerve fibres is severely reduced, and there is a large amount of collagen in the extracellular matrix. Arrowhead: onion bulbs and thinly myelinated nerve fibres.

Taken together, the patients' clinical presentation demonstrates a novel CMT phenotype with two unusual features: (i) aggressive widespread denervation accompanied by concomitant demyelination; and (ii) rapidly progressive and asymmetric weakness without sensory complaints. The clinical presentation and needle EMG imitated MND, although NCS and sural nerve biopsy suggest a demyelinating sensorimotor neuropathy.

Vacuoles interfere with intracellular organelle trafficking in human fibroblasts with FIG4 deficiency

To determine whether FIG4 deficiency is accompanied by vacuolization in patient fibroblasts, as observed in *plt* mice (Chow *et al.*, 2007), we cultured skin fibroblasts from the two CMT4J-patients and an age-matched control. Although control fibroblasts rarely contained vacuoles, many fibroblasts with multiple vacuoles were present in cultures from both patients (Fig. 2A and B). We manually assessed the vacuolization of 529 cells from patient 1 and 201 cells from patient 2, as well as 270 cells from the control culture. The percentage of cells with vacuoles was significantly higher in FIG4-deficient cultures (Fig. 2C).

To investigate the nature and contents of the vacuoles, we labelled cells with antibodies against the late-endosome–lysosome membrane marker LAMP-2 and the early endosome marker EEA1. LAMP-2 was visible on the vacuolar membrane, but EEA1 did not label the vacuoles (Fig. 3C and D). These findings agree with our observations on *plt* mice (Chow *et al.*, 2007), and indicate that the vacuoles are derived from dysfunctioned late-endosomes or lysosomes.

Ubiquitinated inclusions containing excessive phosphorylated neurofilaments (NFp) are a common feature in many neurodegenerative disease (Ballatore *et al.*, 2007). Immunoreactivity against ubiquitin was widespread and evenly distributed in the cytoplasm of motor and sensory neurons in spinal cord and DRG from *plt* mice (Fig. 4A–D). There were no ubiquitinated inclusions within the vacuoles (Fig. 4D, inset). Antibodies against NFp strongly labelled axons but not neuronal cytoplasm or vacuoles (Fig. 4B, inset 4D) There was profound loss of large motor neurons in anterior horns of *plt* mice (4D), consistent with the loss of large diameter motor axons shown in Fig. 5 below.

Mutations of VCP (valosin-containing protein), a regulator of ER protein degradation, result in neuronal vacuolation and degeneration (Ballar *et al.*, 2006). No VCP immunoreactivity was detected in vacuoles in DRG or motor neurons for *plt* mice (arrows in Supplementary Fig. S1).

Vacuoles in *plt* mice were not stained by Filipin (Ko *et al.*, 2001) or Nile red (Schrader, 2001), which detect cholesterol and other lipids (Supplementary Fig. S2). The failure to demonstrate accumulation of lipid or protein within the vacuoles suggests that although these vacuoles originate from late endosomes–lysosomes, they fail to incorporate materials for processing within these organelles.

The abundance of vacuoles in the cell bodies of FIG4-deficient cells suggested that they might physically disrupt trafficking of other intracellular organelles. We performed

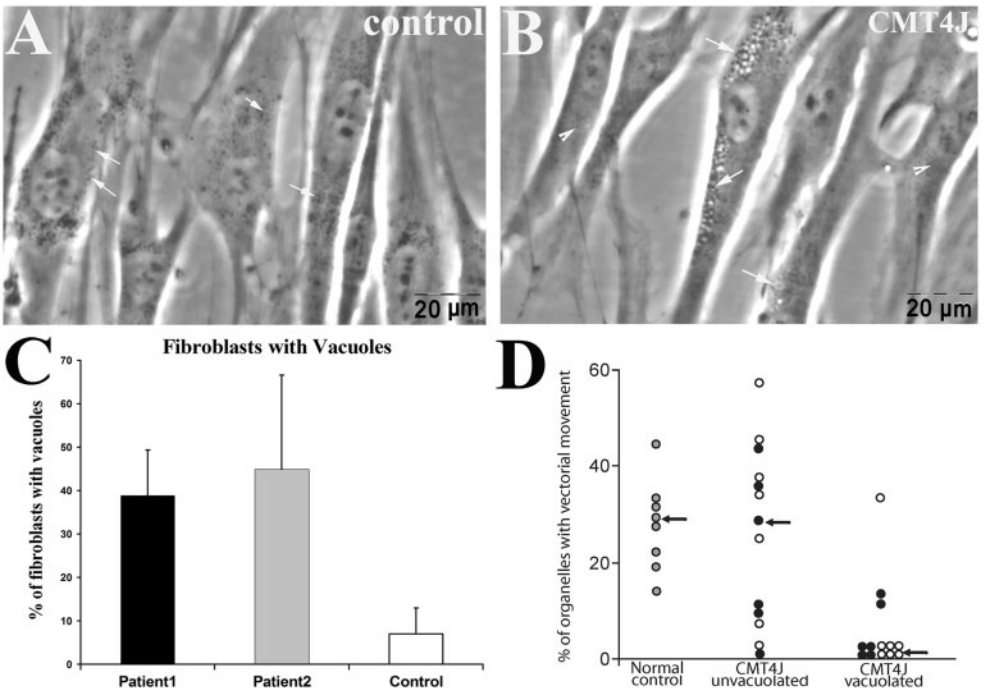

Fig. 2 Vacuolation in FIG4-deficient human fibroblasts. Fibroblasts were isolated from skin biopsies of patients with CMT4J and normal control. Cells were imaged under phase-contrast lens. (**A**) Cultured fibroblasts from the control contained occasional vacuoles. Intracellular organelles appear as 'black-dots' (Waterman-Storer *et al.*, 1999) and are scattered in the cytoplasm (arrows). (**B**) Excessive vacuoles in fibroblasts from patients (arrows). (**C**) Nineteen to twenty two fields from cultures of each human subject were randomly selected under 40× magnification, and the cell number and number of cells with vacuoles were counted. Means ± SD values: 7% ± 6 vacuolated control cells; 39% ± 10 vacuolated cells from patient 1; 45% ± 22 vacuolated cells from patient 2. (**D**) Time lapse imaging was carried out on regions of fibroblasts containing many vacuoles (vacuolated) or lacking vacuoles (non-vacuolated). The percentage of intracellular organelles exhibiting vectorial movement was measured as described in Methods section (Schrader, 2001) ($p = 0.01$ for filled circles; $p = 0.02$ for open circles; compared with non-vacuolated area).

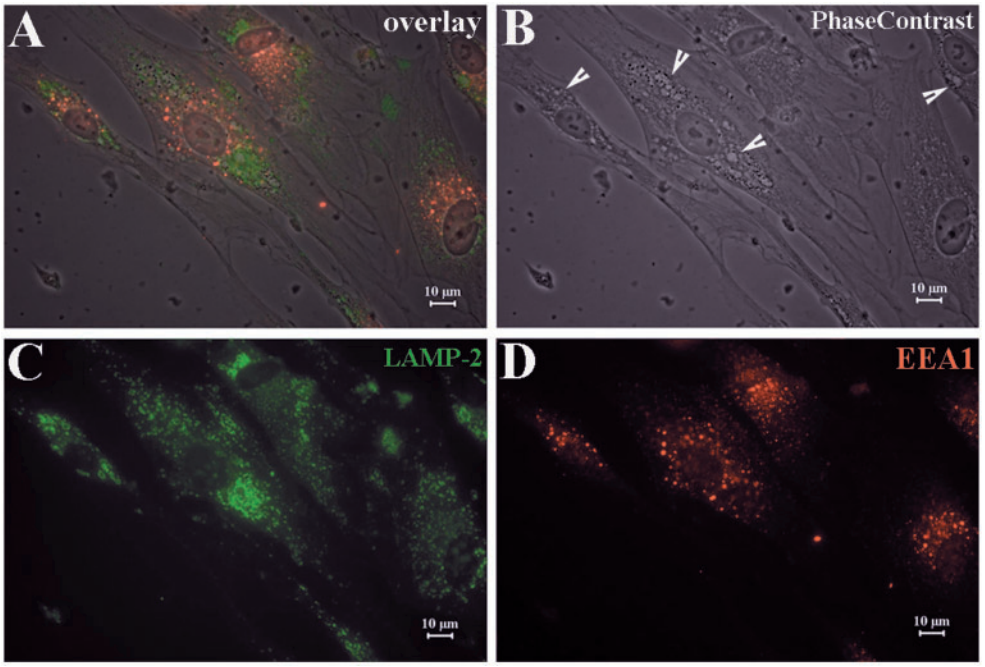

Fig. 3 Vacuoles contain markers for late- endosomes and lysosomes. (**A**) Fibroblasts from human skin biopsies were cultured on glass slides. IHC was then performed on these slides. (**B**) Numerous vacuoles were visualized under phase contrast imaging. (**C**) Cells were stained with antibodies against late-endosome-lysosome marker LAMP-2. (**D**) Cells were stained with antibodies against early endosome marker EEAI. Vacuoles were co-localized with LAMP-2, but not EEAI. This finding is consistent with the observation in mouse fibroblasts (Chow *et al*., 2007) and suggests that the vacuoles are derived from dysfunctional late-endosomes or lysosomes, and not from early endosomes.

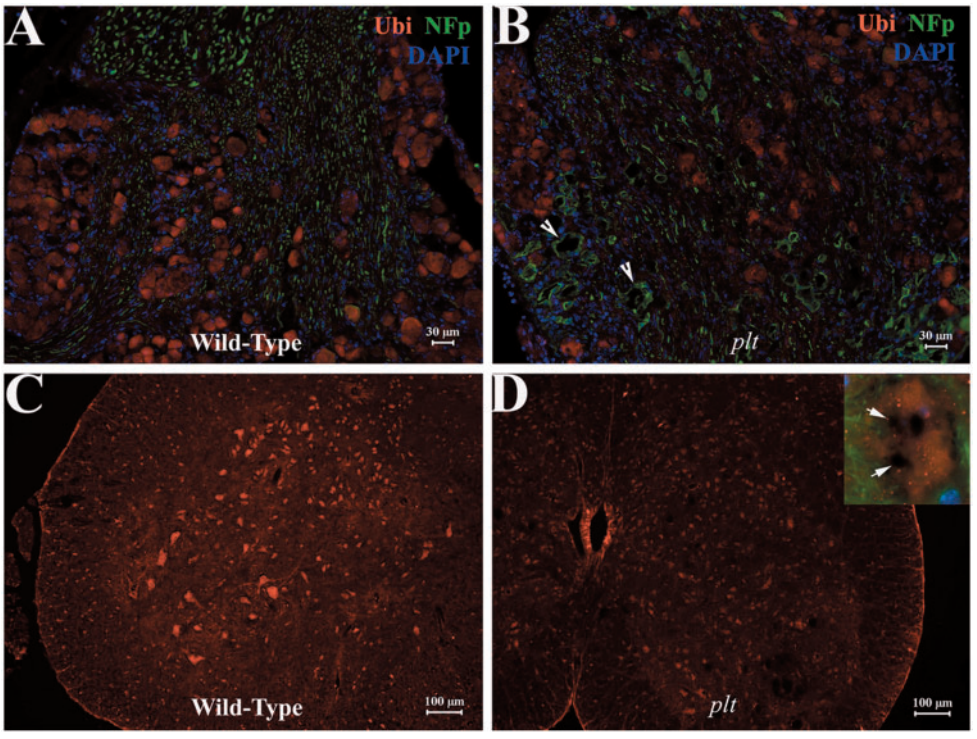

Fig. 4 NF and ubiquitin do not accumulate in neuronal vacuoles. Sections of mouse spinal cord and DRG were examined with IHC technique. (**A–D**) Immunoreactivity against ubiquitin was evenly distributed in the cytoplasm of motor and sensory neurons. Ubiquitinated inclusions were not present in vacuoles. (**A–B**) Antibodies against NFp produced a strong staining in the axons but not in neuronal cytoplasm. Some axons appeared irregular and enlarged (**B**, arrows). Large motor neurons in the anterior horn were reduced in number (5D). Inset: A spinal motor neuron at high magnification lacking NFp and ubiquitin in vacuoles (arrows).

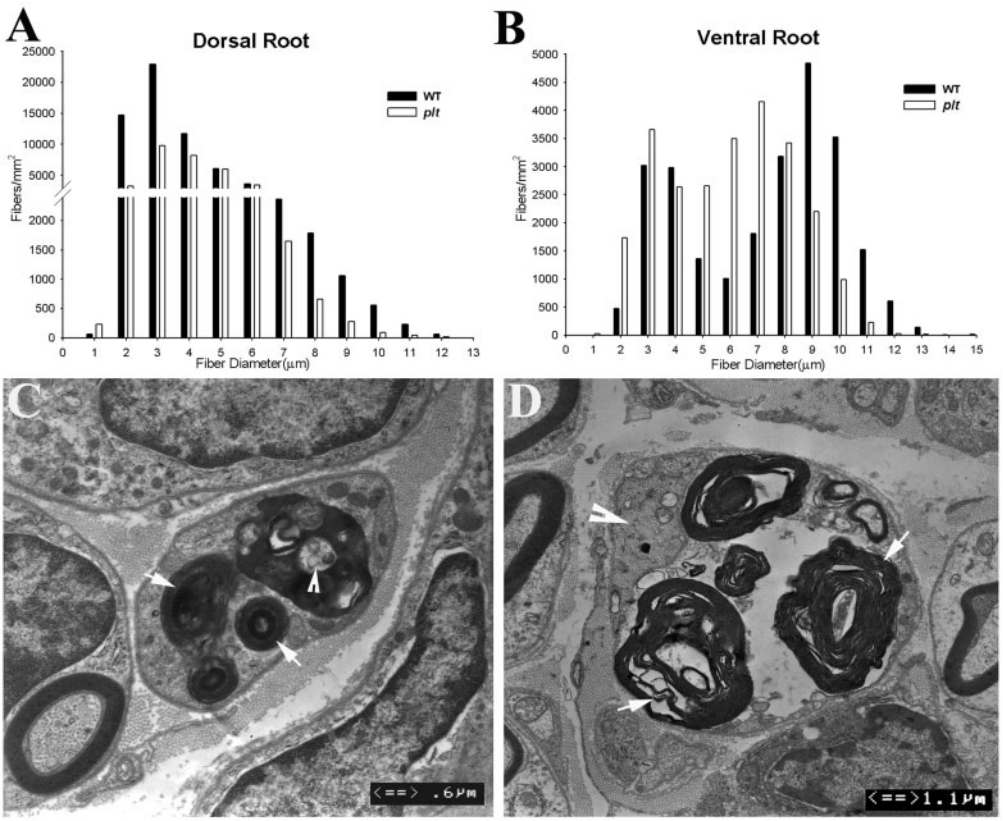

Fig. 5 Axonal degeneration in *plt* mice. Morphometric analysis was performed on the semithin sections of dorsal and ventral roots of 6-week-old *plt* ($n = 4$) and wild-type ($n = 4$) mice (total number of counted myelinated nerve fibres = 3679 for dorsal roots and 2480 for ventral roots in 4 *plt* mice and 4300 for dorsal roots and 2611 for ventral roots in wild-type mice). Sensory nerve fibre loss in the dorsal roots involved both small and large diameter myelinated fibres (**A**). In contrast, axonal loss in the ventral roots mainly affected the large diameter fibres. Small diameter myelinated nerve fibre numbers were increased (**B**). We have also examined femoral, saphenous, tibial and sural nerves under light microscopy (semithin sections) and EM. Active axonal degeneration was conspicuous. Examples are shown in Figs **C** and **D**. In (**C**), a degenerated nerve fibre is in the centre of the picture. Myelin debris is localized in the Schwann cell cytoplasm (arrows). An axon-like residue is visible (arrowhead), presumably from a degenerated axon. A similar nerve fibre is shown in (**D**). Again, myelin debris is prominent (arrows in **D**). The axon is still preserved, but appears irregular with condensed cytoskeletons and intra-axonal organelles (arrowhead).

time-lapse imaging on cultured fibroblasts isolated from patient skin biopsies over 30 min and quantified movement during a 5 min period of observation (Schrader, 2001). In control fibroblasts vacuoles were rarely visible. Many organelles exhibited fast movement in long trajectories towards or away from the nucleus. In contrast, FIG4-deficient fibroblasts contain many stationary vacuoles, often clustered in the perinuclear region of the cell. Organelle movement was normal in regions of mutant cells lacking vacuoles, but was severely limited around and between vacuoles (Supplementary Video 5).

To quantify the organelle motility defect, we randomly placed three $4 \times 4\,\mu M$ 'interest boxes' in each fibroblast captured by time-lapse imaging. Intracellular organelles were manually counted and categorized by their motility features as has been previously described (Ko *et al.*, 2001). Stationary organelles lacked any movements over a 5 min period; vectorial organelles were observed to move in long paths either toward or away from nucleus; Brownian organelles, displayed short, continuous back-and-forth movements (Ko *et al.*, 2001). Stationary organelles accounted for ~20% of the total organelles in control cells and in the non-vacuolated regions of mutant cells. In the areas that were heavily vacuolated, 60–80% of organelles were stationary (Supplementary Table S1). There was a decrease in organelles exhibiting vectorial movement from ~30% in control cells to 5% in vacuolated regions of mutant cells (Fig. 2D). In the non-vacuolated areas, there was no difference in the percentages of any movements between FIG4-deficient fibroblasts and control fibroblasts (Supplementary Table S1). These findings suggest that the trafficking of intracellular organelles is blocked or prevented by the clustered vacuoles in FIG4-deficient cells (a regional impairment) since there were no trafficking abnormalities in non-vacuolated areas. Since there is extensive vacuolation in *plt* neurons as well (Chow *et al.*, 2007), obstruction of intracellular organelle trafficking may contribute to neuronal degeneration in mice and CMT4J patients.

Neuronal degeneration in *plt* mice

plt mice exhibit severe neuronal degeneration and neuronal vacuolization in brain, spinal cord and sensory ganglia (Chow *et al.*, 2007). The disease is progressive over a 6-week period resulting in juvenile death. To better characterize the degeneration in the PNS we performed morphometric analysis of dorsal and ventral roots. At 6 weeks of age, sensory nerve fibre loss in the dorsal roots affected both small and large diameter myelinated fibres (Fig. 5A). Axonal loss in the ventral roots mainly affected the large diameter fibres (Fig. 5B). The number of small diameter nerve fibres ($\leqslant$4 μm) was increased by 25% in the ventral roots, possibly due to collateral branch regeneration. At 3 weeks of age, degenerating axons were visible in femoral (primarily motor), saphenous (primarily sensory) and tibial (mixed) nerves (Fig. 5C and D). The data demonstrate degeneration of both motor and sensory axons in *plt* mice.

Evaluation of apoptosis and cell proliferation in *plt* mice

To determine whether apoptosis contributes to neuronal loss in FIG4 deficiency, we performed TUNEL staining on sections from DRG, spinal cord, sciatic nerve and dorsal root of 6-week-old *plt* mice. TUNEL staining was readily detected in control tumour cells, but there was no or negligible staining in mutant tissues and no significant difference from wild-type mice (Supplementary Fig. S3). There thus was no increase in apoptosis of neurons and Schwann cells of *plt* mice at this age.

The same tissues were stained with antibodies to Ki67 to assess cell proliferation (Muskhelishvili *et al.*, 2003). No significant difference was observed between wild-type and *plt* tissues (Supplementary Fig. S4). As a positive control, strong Ki67 immunoreactivity was detected in hair follicles of the skin biopsies, an anatomical region with abundant proliferating cells (Morris *et al.*, 2004).

Segmental demyelination in *plt* mice

The reduced conduction velocity in nerves of patients (Table 2) and *plt* mice (Chow *et al.*, 2007) was suggestive of segmental demyelination. Therefore, we examined teased nerve fibres from sciatic nerves of *plt* mice. Schwann cell-specific MAG (myelin-associated glycoprotein) was present in myelenated neurons and was strongly expressed in Schmidt-Lantermann incisures (Fig. 6A). In some segments of myelinated nerve fibres there was an absence of MAG staining, demonstrating segmental demyelination (Fig. 6B). Segmental demyelination was observed in 11% of a random selection of 100 myelinated nerve fibres from *plt* mice, but was not detected in wild-type fibres.

Macrophages containing debris, presumably from engulfed myelin, were visible in dorsal roots of mutant mice (arrowheads in Fig. 7B). The identity of macrophages was confirmed using CD68 antibodies (Supplementary Fig. S5). Myelinated nerve fibres from the mutant mice exhibited thin myelin, absence of myelin or basal lamina redundancy (Fig. 7C and D). Myelin debris was occasionally seen in Schwann cells (7E). Vacuoles were abundant in the perinuclear region of neuronal bodies, but were rarely

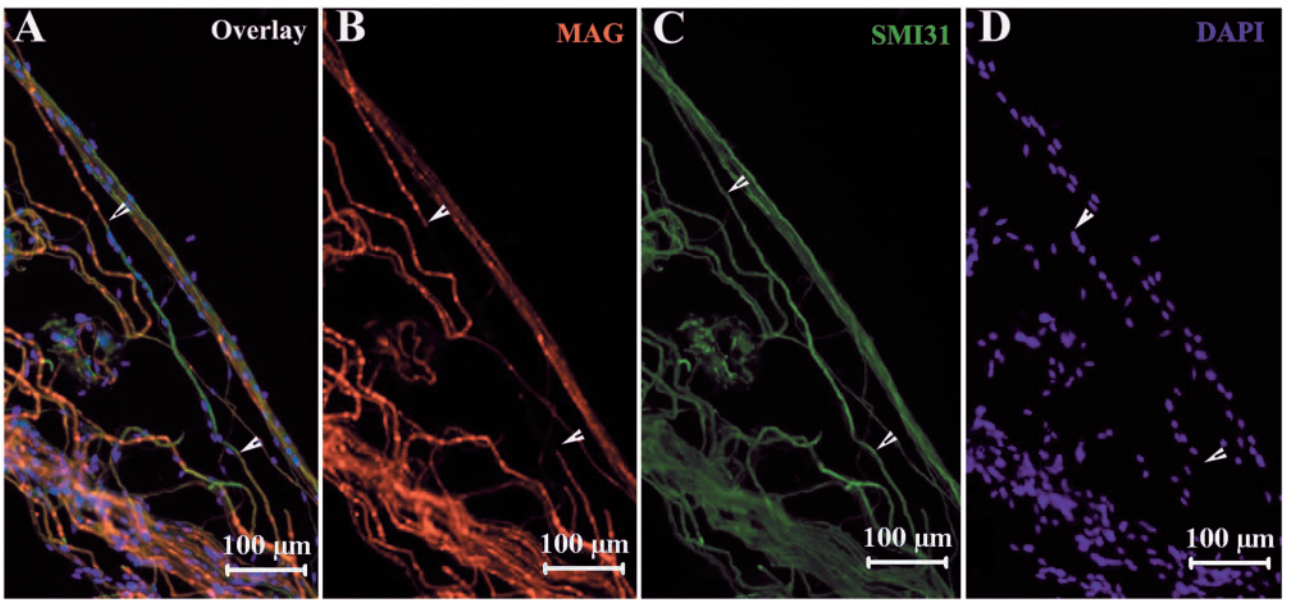

Fig. 6 Segmental demyelination in teased sciatic nerve fibres from *plt* mice. Mouse sciatic nerves were teased into individual glass slides and stained with IHC techniques. (**A**) Myelin specific protein MAG was strongly expressed in Schmidt-Lantemann incisures. MAG staining was absent in some segments of myelinated nerve fibres (e.g. between arrowheads in **A, B**). Labelling for NFp was intact in the same segment (**C**), demonstrate segmental demyelination. Many nuclei were lined up along this segment of the axon (**D**) derived from invading macrophages or remyelinating Schwann cells. Demyelination was not observed in wild-type nerve fibres.

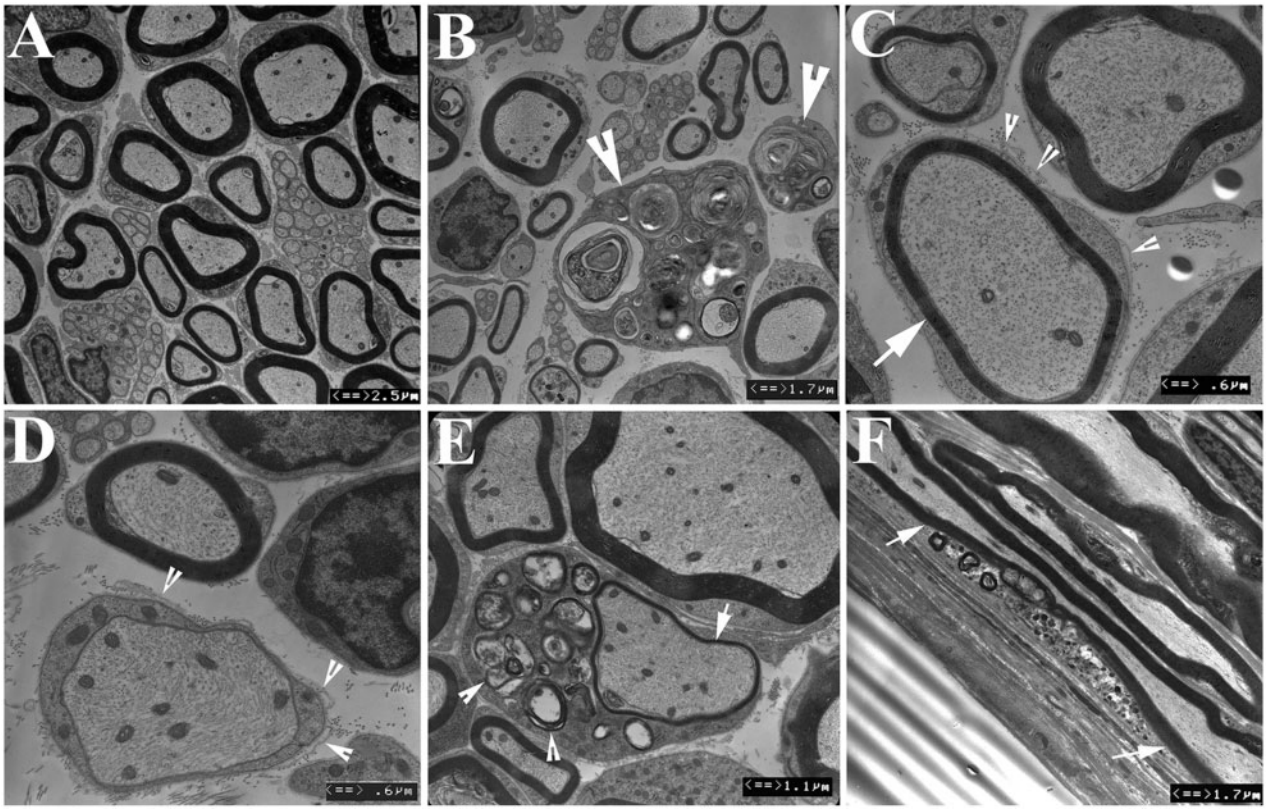

Fig. 7 Demyelination confirmed by ultrastructure. Peripheral nerves were prepared into ultrathin sections and examined under EM. (**A**) Sciatic nerves from wild-type mice exhibited myelinated nerve fibres of various diameter as well as non-myelinated fibres. (**B**) Sciatic nerves from *plt* mice showed significantly reduced density of myelinated nerve fibres. Macrophages were present in dorsal roots but less frequently in other nerves (arrowheads). Macrophage cytoplasm contained debris, presumably from engulfed myelin. Nerve fibres with thin myelin (arrow in **C**) or absence of myelin (**D**) were observed. Many had basal lamina redundancy (arrowheads in **C** and **D**), a pathological change suggesting remyelination. (**E**) Myelin debris was occasionally observed in Schwann cell cytoplasm (arrowheads), suggesting active demyelination/remyelination. (**F**) Myelination debris in a segment of myelinated nerve fibre (between arrows) can also be seen in longitudinal sections of nerves. Vacuoles were restricted to neuronal soma and not present in axons or Schwann cells. The ultrastructural changes are consistent with the IHC findings in Fig. 6 supporting segmental demyelination in *plt* mice.

Table 3 Morphometric analysis of myelinated nerve fibre myelin thickness in the dorsal and ventral roots of *plt* and wild-type mice (mean ± SD, $n = 4$ mice for each genotype)

	Ventral Root			Dorsal Root		
Diameter	*g*-ratio	Myelin thickness	*P*-value	*g*-ratio	Myelin thickness	*P*-value
wt < 4 μm	0.45 ± 0.05	1.93 ± 0.39	0.068^{g}	0.51 ± 0.01	1.18 ± 0.03	0.058^{g}
Plt < 4 μm	0.52 ± 0.04	1.47 ± 0.28	0.104^{m}	0.55 ± 0.03	1.47 ± 0.12	$\mathbf{0.049}^{m}$
wt ⩾ 4 μm	0.53 ± 0.05	2.28 ± 0.32	$\mathbf{0.048}^{g}$	0.59 ± 0.03	1.77 ± 0.19	$\mathbf{0.019}^{g}$
Plt ⩾ 4 μm	0.60 ± 0.03	1.60 ± 0.28	$\mathbf{0.019}^{m}$	0.65 ± 0.03	1.31 ± 0.23	$\mathbf{0.023}^{m}$

g, *P*-value for *g*-ratio comparison between *wt* and *plt* mice. *G*-ratio = the numerical ratio between the diameter of the axon proper and the outer diameter of the myelinated fibre; *m*, *P*-value for myelin thickness comparison between *wt* and *plt* mice.

observed in Schwann cells and never in axons. Excessive myelin out-folding was not observed in *plt* mice, in contrast to *MTMR2*/13 deficient patients and mice (Bolino *et al.*, 2004; Robinson *et al.*, 2005; Tersar *et al.*, 2007). Taken together, the ultrastructural changes and the IHC findings in Fig. 6 demonstrate segmental demyelination in peripheral nerves. Consistent with this result, morphometric analysis of the dorsal and ventral roots revealed an increased g-ratio and decreased myelin thickness in the large diameter (⩾4 μM) myelinated nerve fibres (Table 3).

Discussion

We describe a novel phenotype of rapidly progressive and asymmetric paralysis in two patients with mutations in *FIG4*. The pattern of regional progression is distinct from

typical CMT, which exhibits slowly progressive, symmetric, length-dependent polyneuropathy. CMT4J more closely resembles MND, a disorder also characterized by rapidly progressive asymmetric weakness in which symptoms move from one limb to the contralateral limb before progressing to the other extremities (Caroscio *et al.*, 1987; Brooks *et al.*, 1995). CMT4J patients exhibit no sensory symptoms and minimal signs of sensory loss on neurological examination. The reasons for this are unclear since there is evidence of physiological and morphological sensory nerve involvement in both patients and mice. Taken together, the clinical progression and electrophysiological finding of active denervation with massive fibrillations and positive waves are consistent with an aggressive neuronopathy, as distinguished from polyneuropathy characterized by chronic, symmetric, length-dependent denervation.

The mechanism of rapid and asymmetric progression in CMT4J is not understood. In both CMT4J patients, the initially affected limb experienced minor trauma that preceded the development of marked weakness. Over several years the weakness rapidly progressed to the other limbs. Although the trauma could be coincidental in the two patients, trauma has been hypothesized to influence neurodegeneration in a number of disorders (Chio *et al.*, 2005; Hachiya *et al.*, 2007). Alternatively, the falls taken by both patients near the onset of progression may have resulted from the prior development of subclinical weakness. Uneven distribution of vacuolated motor neurons in the spinal cord could contribute to the asymmetric progression in our patients. Whatever the explanation, FIG4 deficiency may provide a unique opportunity to investigate the molecular mechanisms underlying asymmetric progression in MND.

Time-lapse imaging of cultured CMT4J fibroblasts suggested a potential cellular mechanism for the clinical disorder: defective trafficking of intracellular organelles due to obstruction by vacuoles. Trafficking of intracellular organelles is essential for cell survival. Maintenance of an energy supply, for example, requires mitochondrial transport within cells. Impaired trafficking could affect survival, particularly for polarized neurons with long axons (Baloh *et al.*, 2007). Vacuoles were observed only in the neuronal cell body, and not in the axons, indicating that there is impaired organelle trafficking in the cell body. This is consistent with the fact that weakness was not length dependent in our patients. The possibility of a direct or secondary effect on axonal transport has not been investigated. Impaired organelle trafficking has been implicated in the pathogenesis of other MNDs. For example, mutations of the vesicle-associated membrane protein-associated protein-B (VAPB) gene are responsible for an inherited form of amyotrophic lateral sclerosis and spinal muscular atrophy [Nishimura *et al.*, 2004; Marques *et al.*, 2006]. VAPB is localized on endoplasmic reticulum and Golgi apparatus, where it regulates organelle transport and interacts with lipid-binding proteins. VAPB levels are also reduced in patients with sporadic amyotrophic lateral sclerosis (Nishimura *et al.*, 2004; Marques *et al.*, 2006).

Vacuole formation in FIG4 deficient cells appears to involve the endocytic pathway. Endocytic trafficking requires coordinated signalling by PI3P, which plays a crucial role in the formation of early endosomes (Volpicelli-Daley *et al.*, 2007), and $PI(3,5)P_2$, which may trigger budding of vesicles from late endosomes (Efe *et al.*, 2005; Di Paolo *et al.*, 2006; Rutherford *et al.*, 2006). Reduced $PI(3,5)P_2$ due to loss of function of *FIG4* could inhibit budding, leading to the accumulation of large vesicles in the endocytic compartment (Marks, 2008). This model is supported by the presence of LAMP2, a marker of late endosomes and early lysosomes, on the enlarged vacuoles in cultured fibroblasts from human patients (this article) and the *plt* mouse (Chow *et al.*, 2007).

It is intriguing that vacuoles are rarely observed in Schwann cells although they are abundant in neurons. Differential effects on neurons and Schwann cells have been observed for mutations of other genes in the phosphoinositide pathway. *Mtmr2* encodes a phosphatase that dephosphorylates the 3-position of $PI(3,5)P_2$. Mutations of human *MTMR2* result in CMT4B1 (Bolino *et al.*, 2000; Suter 2007). Conditional inactivation of *Mtmr2* in Schwann cells in the mouse recapitulates the pathology of CMT4B1, while inactivation in motor neurons had no effect (Bolis *et al.*, 2005). There thus appear to be differences in phosphoinositide signalling in the two cell types.

Despite their low level of vacuolization, Schwann cells are likely to be responsible for the observed segmental demyelination. However, this mild demyelination is unlikely to be a major cause of disability, since the pattern of rapid asymmetric progress is characteristic of neuronopathy. Abnormal Schwann cell-axonal interactions may also contribute to the axonal loss. Altered interactions between Schwann cells and axons occur in many demyelinating neuropathies. For instance, trembler mice with a Pmp22 missense mutation (Suter *et al.*, 1992) have decreased NF-phosphorylation and axonal transport in addition to demyelination (de Waegh *et al.*, 1990; de Waegh *et al.*, 1992; Watson *et al.*, 1994). Similarly, the myelin protein zero mutations T95M and H10P produced axonal neuropathy with minimal demyelination (De Jonghe *et al.*, 1999; Bai *et al.*, 2006; Li *et al.*, 2006). Axonal degeneration in all of these models is chronic, symmetric and length dependent. None of these features are characteristic of mice or patients with FIG4 deficiency.

The pathological evidence of segmental demyelination in the two patients and in *plt* mice is consistent with the reduced nerve conduction velocities. The striking difference in conduction velocity between the two patients may reflect a different extent of segmental demyelination, which could result from genetic differences in modifying genes. In spite of the difference in conduction velocity, the clinical deficits in the two patients are very similar.

In contrast to the severe neuronal degeneration in the CNS of *plt* mice (Chow *et al.*, 2007), we found no upper motor neuron signs in the patients with CMT4J. One patient had an unremarkable brain MRI. Detailed psychometric tests were not performed but, there was no obvious cognitive dysfunction in either patient, both of whom had successful professional careers. Thus, any CNS abnormalities were subtle. The partial function of the I41T variant of FIG4 may protect the CNS of patients from the degeneration seen in the null *plt* mice, and may also explain the normal pigmentation in patients with CMT4J. It is possible that differences in PI(3,5)P_2 signalling between human and mouse also contribute to the phenotypic differences.

Supplementary material

Supplementary material is available at *Brain* online.

Acknowledgements

Authors thank Dr Istvan Katonia and Ms Yanmei Yuan for technical assistance. This research is supported by grants from the NINDS (K08 NS048204), NIGMS (R01 GM24872), MDA (MDA 4029) and the Hiller ALS foundation. We would like to especially thank the family involved for their contributions to this study.

References

Bai YH, Ianokova E, Pu Q, Ghandour K, Levinson R, Martin JJ, et al. R69C Mutation in P0 Gene alters myelination and ion channel subtypes. Arch Neurol 2006; 63: 1787–94.

Ballar P, Shen Y, Yang H, Fang S. The role of a novel p97/valosin-containing protein-interacting motif of gp78 in endoplasmic reticulum-associated degradation. J Biol Chem 2006; 281: 35359–68.

Ballatore C, Lee VM, Trojanowski JQ. Tau-mediated neurodegeneration in Alzheimer's disease and related disorders. Nat Rev Neurosci 2007; 8: 663–72.

Baloh RH, Schmidt RE, Pestronk A, Milbrandt J. Altered axonal mitochondrial transport in the pathogenesis of Charcot-Marie-Tooth disease from mitofusin 2 mutations. J Neurosci 2007; 27: 422–30.

Barber RP, Phelps PE, Houser CR, Crawford GD, Salvaterra PM, Vaughn JE. The morphology and distribution of neurons containing choline acetyltransferase in the adult rat spinal cord: an immunocytochemical study. J Comp Neurol 1984; 229: 329–46.

Bolino A, Bolis A, Previtali SC, Dina G, Bussini S, Dati G, et al. Disruption of Mtmr2 produces CMT4B1-like neuropathy with myelin outfolding and impaired spermatogenesis. J Cell Biol 2004; 167: 711–21.

Bolino A, Muglia M, Conforti FL, LeGuern E, Salih MA, Georgiou DM, et al. Charcot-Marie-Tooth type 4B is caused by mutations in the gene encoding myotubularin-related protein-2. Nat Genet 2000; 25: 17–9.

Bolis A, Coviello S, Bussini S, Dina G, Pardini C, Previtali SC, et al. Loss of Mtmr2 phosphatase in Schwann cells but not in motor neurons causes Charcot-Marie-Tooth type 4B1 neuropathy with myelin outfoldings. J Neurosci 2005; 25: 8567–77.

Bolis A, Zordan P, Coviello S, Bolino A. Myotubularin-related (MTMR) phospholipid phosphatase proteins in the peripheral nervous system. Mol Neurobiol 2007; 35: 308–16.

Brooks BR, Shodis KA, Lewis DH, Rawling JD, Sanjak M, Belden DS, et al. Natural history of amyotrophic lateral sclerosis. Quantification of symptoms, signs, strength, and function. Adv Neurol 1995; 68: 163–84.

Caroscio JT, Mulvihill MN, Sterling R, Abrams B. Amyotrophic lateral sclerosis. Its natural history. Neurol Clin 1987; 5: 1–8.

Chio A, Benzi G, Dossena M, Mutani R, Mora G. Severely increased risk of amyotrophic lateral sclerosis among Italian professional football players. Brain 2005; 128: 472–6.

Chow CY, Zhang Y, Dowling JJ, Jin N, Adamska M, Shiga K, et al. Mutation of FIG4 causes neurodegeneration in the pale tremor mouse and patients with CMT4J. Nature 2007; 448: 68–72.

da Silva RP, Gordon S. Phagocytosis stimulates alternative glycosylation of macrosialin (mouse CD68), a macrophage-specific endosomal protein. Biochem J 1999; 338: 687–94.

De Jonghe P, Timmerman V, Ceuterick C, Nelis E, De Vriendt E, Löfgren A, et al. The Thr124Met mutation in the peripheral myelin protein zero (MPZ) gene is associated with a clinically distinct Charcot-Marie-Tooth phenotype. Brain 1999; 122: 281–90.

de Waegh S, Brady ST. Altered slow axonal transport and regeneration in a myelin-deficient mutant mouse: the trembler as an in vivo model for Schwann cell-axon interactions. J Neurosci 1990; 10: 1855–65.

de Waegh SM, Lee VM, Brady ST. Local modulation of neurofilament phosphorylation, axonal caliber, and slow axonal transport by myelinating Schwann cells. Cell 1992; 68: 451–63.

Di Paolo G, De Camilli P. Phosphoinositides in cell regulation and membrane dynamics. Nature 2006; 443: 651–7.

Duex JE, Nau JJ, Kauffman EJ, Weisman LS. Phosphoinositide 5-phosphatase Fig 4p is required for both acute rise and subsequent fall in stress-induced phosphatidylinositol 3,5-bisphosphate levels. Eukaryot Cell 2006a; 5: 723–31.

Duex JE, Tang F, Weisman LS. The Vac14p-Fig4p complex acts independently of Vac7p and couples PI3,5P2 synthesis and turnover. J Cell Biol 2006b; 172: 693–704.

Efe JA, Botelho RJ, Emr SD. The Fab1 phosphatidylinositol kinase pathway in the regulation of vacuole morphology. Curr Opin Cell Biol 2005; 17: 402–8.

Eisen A. Clinical electrophysiology of the upper and lower motor neuron in amyotrophic lateral sclerosis. Semin Neurol 2001; 21: 141–54.

Fanin M, Nascimbeni AC, Fulizio L, Spinazzi M, Melacini P, Angelini C. Generalized lysosome-associated membrane protein-2 defect explains multisystem clinical involvement and allows leukocyte diagnostic screening in Danon disease. Am J Pathol 2006; 168: 1309–20.

Giasson BI, Mushynski WE. Aberrant stress-induced phosphorylation of perikaryal neurofilaments. J Biol Chem 1996; 271: 30404–9.

Goldstein ME, House SB, Gainer H. NF-L and peripherin immunoreactivities define distinct classes of rat sensory ganglion cells. J Neurosci Res 1991; 30: 92–104.

Gonzalez-Martinez T, Perez-Piñera P, Díaz-Esnal B, Vega JA. S-100 proteins in the human peripheral nervous system. Microsc Res Tech 2003; 60: 633–8.

Hachiya NS, Kozuka Y, Kaneko K. Mechanical stress and formation of protein aggregates in neurodegenerative disorders. Med Hypotheses 2008; 70: 1034–7.

Ko DC, Gordon MD, Jin JY, Scott MP. Dynamic movements of organelles containing Niemann-Pick C1 protein: NPC1 involvement in late endocytic events. Mol Biol Cell 2001; 12: 601–14.

Li J, Bai YH, Anokova E, Grandis M, Uchwat F, Trostinskaia A, et al. Major myelin protein gene (P0) mutation causes a novel form of axonal degeneration. J Comp Neurol 2006; 498: 252–65.

Li J, Petajan J, Smith G, Bromberg M. Electromyography of sternocleidomastoid muscle in ALS: a prospective study. Muscle Nerve 2002; 25: 725–8.

Marks MS. FIG4, Charcot-Marie-Tooth disease, and hypopigmentation: a role for phosphoinositides in melanosome biogenesis? Pigment Cell Melanoma Res 2008; 21: 11–4.

Marques VD, Barreira AA, Davis MB, Abou-Sleiman PM, Silva WA Jr, Zago MA, et al. Expanding the phenotypes of the Pro56Ser VAPB mutation: proximal SMA with dysautonomia. Muscle Nerve 2006; 34: 731–9.

Mills IG, Jones AT, Clague MJ. Involvement of the endosomal autoantigen EEA1 in homotypic fusion of early endosomes. Curr Biol 1998; 8: 881–4.

Morris RJ, Liu Y, Marles L, Yang Z, Trempus C, Li S, et al. Capturing and profiling adult hair follicle stem cells. Nat Biotechnol 2004; 22: 411–7.

Muskhelishvili L, Latendresse JR, Kodell RL, Henderson EB. Evaluation of cell proliferation in rat tissues with BrdU, PCNA, Ki-67(MIB-5) immunohistochemistry and in situ hybridization for histone mRNA. J Histochem Cytochem 2003; 51: 1681–8.

Nishimura AL, Mitne-Neto M, Silva HC, Richieri-Costa A, Middleton S, Cascio D, et al. A mutation in the vesicle-trafficking protein VAPB causes late-onset spinal muscular atrophy and amyotrophic lateral sclerosis. Am J Hum Genet 2004; 75: 822–31.

Robinson FL, Dixon JE. The phosphoinositide-3-phosphatase MTMR2 associates with MTMR13, a membrane-associated pseudophosphatase also mutated in type 4B Charcot-Marie-Tooth disease. J Biol Chem 2005; 280: 31699–707.

Rutherford AC, Traer C, Wassmer T, Pattni K, Bujny MV, Carlton JG, et al. The mammalian phosphatidylinositol 3-phosphate 5-kinase (PIKfyve) regulates endosome-to-TGN retrograde transport. J Cell Sci 2006; 119: 3944–57.

Sbrissa D, Ikonomov OC, Fu Z, Ijuin T, Gruenberg J, Takenawa T, et al. Core protein machinery for mammalian phosphatidylinositol 3,5-bisphosphate synthesis and turnover that regulates the progression of endosomal transport. Novel Sac phosphatase joins the ArPIKfyve-PIKfyve complex. J Biol Chem 2007; 282: 23878–91.

Schrader M. Tubulo-reticular clusters of peroxisomes in living COS-7 cells: dynamic behavior and association with lipid droplets. J Histochem Cytochem 2001; 49: 1421–9.

Suter U. Phosphoinositides and Charcot-Marie-Tooth disease: new keys to old questions. Cell Mol Life Sci 2007; 64: 3261–5.

Suter U, Moskow JJ, Welcher AA, Snipes GJ, Kosaras B, Sidman RL, et al. A leucine-to-proline mutation in the putative first transmembrane domain of the 22-kDa peripheral myelin protein in the trembler-J mouse. Proc Natl Acad Sci USA 1992; 89: 4382–6.

Tersar K, Boentert M, Berger P, Bonneick S, Wessig C, Toyka KV, et al. Mtmr13/Sbf2-deficient mice: an animal model for CMT4B2. Hum Mol Genet 2007; 16: 2991–3001.

Thompson RL, Sawtell NM. HSV latency-associated transcript and neuronal apoptosis. Science 2000; 289: 1651.

Vij N, Fang S, Zeitlin PL. Selective inhibition of endoplasmic reticulum-associated degradation rescues DeltaF508-cystic fibrosis transmembrane regulator and suppresses interleukin-8 levels: therapeutic implications. J Biol Chem 2006; 281: 17369–78.

Volpicelli-Daley L, De Camilli P. Phosphoinositides' link to neurodegeneration. Nat Med 2007; 13: 784–6.

Waterman-Storer CM, Worthylake RA, Liu BP, Burridge K, Salmon ED. Microtubule growth activates Rac1 to promote lamellipodial protrusion in fibroblasts. Nat Cell Biol 1999; 1: 45–50.

Watson DF, Nachtman FN, Kuncl RW, Griffin JW. Altered neurofilament phosphorylation and beta tubulin isotypes in Charcot-Marie-Tooth disease type 1. Neurology 1994; 44: 2383–7.

Yamamoto Y, Mizuno R, Nishimura T, Ogawa Y, Yoshikawa H, Fujimura H, et al. Cloning and expression of myelin-associated oligodendrocytic basic protein. A novel basic protein constituting the central nervous system myelin. J Biol Chem 1994; 269: 31725–30.

Yan Y, Jensen K, Brown A. The polypeptide composition of moving and stationary neurofilaments in cultured sympathetic neurons. Cell Motil Cytoskeleton 2007; 64: 299–309.